A Ni-MoO$_x$ composite catalyst for the hydrogen oxidation reaction in anion exchange membrane fuel cell

YongKeun Kwon [a], Doosun Hong [a], Jue-Hyuk Jang [b], MinJoong Kim [c], SeKwon Oh [d], DongHoon Song [a], JeongHoon Lim [a], Sung Jong Yoo [b], EunAe Cho [a,*]

[a] Department of Materials Science and Engineering, Korea Advanced Institute of Science and Technology, 291 Daehak-Ro, Yuseong-gu, Daejeon, Republic of Korea
[b] Fuel Cell Research Center, Korea Institute of Science and Technology, 5, Hwarang-ro 14 gil, Seongbuk-gu, Seoul, Republic of Korea
[c] Hydrogen Research Department, Korea Institute of Energy Research, 152 Gajeong-ro, Yuseong-gu, Daejeon, Republic of Korea
[d] Heat & Surface Technology R&D Department, Korea Institute of Industrial Technology, Incheon 21999, Republic of Korea

ARTICLE INFO

ABSTRACT

In developing anion exchange membrane fuel cells (AEMFCs), the sluggish hydrogen oxidation reaction (HOR) under alkaline condition is one of the major challenges to be overcome. A screening process using the simple electrodeposition method suggests Ni-29Mo as the most promising composition among the prepared Ni-M (M= Co, Fe, Zn, Cr, Mo, W) and Ni-xMo (x = 22~33 at%) samples. Experimental analyses and theoretical computations demonstrate that the Ni-29Mo is composed of metallic nickel and molybdenum oxide (Ni-MoO$_x$) domains and the hydrogen adsorption energy on metallic Ni is tailored in the presence of MoO$_2$ towards the optimal value. The Ni-MoO$_x$ composite catalyst shows a superior HOR activity (1.12 mA/cm^2 @ 20 mV$_{RHE}$), outperforming carbon supported platinum (Pt/C, 1.01 mA/cm^2 @ 20 mV$_{RHE}$), the best HOR catalyst. An AEMFC fabricated using Ni-29Mo nanoparticles as an anode catalyst exhibits excellent performance, approximately half of the Pt/C counterpart cell, demonstrating practical applicability of the catalyst.

1. Introduction

Proton exchange membrane fuel cell (PEMFC) is a power source that can generate electricity and heat by the electrochemical reaction between hydrogen and oxygen with a high efficiency. Since a PEMFC produces only water as a byproduct without emission of carbon dioxide and any other air pollutants, it is considered an environmental-friendly device [1]. Currently, PEMFCs are commercialized as power generators for passenger vehicles and residential usage. However, the growth of the PEMFC market is being limited by the high fabrication cost, which is mainly attributed to the use of platinum (Pt)-based catalysts particularly for the sluggish oxygen reduction reaction (ORR) at the cathode. To reduce Pt usage or to replace Pt with non-precious group metal (non-PGM) catalysts, extensive studies have been conducted and reported improved ORR activities [2–7]. However, due to the crucial durability issues [8,9], PEMFCs are still utilizing the conventional Pt-based catalysts [10].

As an alternative to PEMFCs, anion exchange membrane fuel cells (AEMFCs) have been developed. In an alkaline condition, the ORR

kinetics is significantly enhanced even on non-precious catalysts [11, 12]. Thus, the production cost can be dramatically reduced by removing precious catalysts from the cathode [13,14]. However, in addition to the poor stability of the anion exchange membranes, a sluggish hydrogen oxidation reaction (HOR) should be overcome for implementation of AEMFCs [15,16]. Pt is known as the best catalyst for the HOR in an acid condition [17]. In alkaline condition, which includes a hydroxyl anion as an intermediate of HOR, the mechanism is different from that in the acid condition and the catalytic activity of Pt substantially decreases [16]. Previous studies reported that the reduced HOR activity of Pt can be attributed to the weak OH adsorption energy [15] or weak hydrogen binding energy (HBE) [18] in the alkaline condition. In addition, it has been presented that alloying Pt with ruthenium (Ru) effectively enhances the HOR activity in the alkaline condition [18,19].

As a non-PGM HOR catalyst, nickel (Ni) has been widely utilized for the anode of alkaline fuel cells (AFCs). Raney-Ni [20,21], a well-known organic hydrogenation catalyst with high surface area, has been widely employed as a catalyst for the AFC anode. However, HOR activity of Ni-based catalysts was lower than that of Pt, mostly due to the strong

HBE of Ni compared to the optimum value [22,23]. To tune the HBE, Ni has been alloyed with cobalt (Co) and molybdenum (Mo) or supported on nitrogen (N)-doped carbon nanotube (CNT) [24,25]. In addition, bimetallic Ni_4Mo and Ni_4W nanoalloys (Ni_4Mo/W) [26], metal-organic framework (MOF)-derived composites composed of Ni, Ni-oxide and carbon (Ni/NiO/C) [27], carbon-supported Ni and copper alloy nanoparticles (NiCu/C) [28] were also investigated to enhance the catalytic activity of Ni. However, most of the previous studies evaluated the HOR activity using a half-cell configuration with an alkaline solution rather than preparing a membrane-electrode assembly (MEA) for AEMFC. From the extensive studies on PEMFC catalysts, it is well known that fabrication of MEAs using a newly-developed catalyst is highly challenging due to the difficulties in controlling the microstructure of the electrode composed of nanometer-sized catalyst and ionomer [29]. Thus, only few non-precious catalysts reported AEMFC performance [30].

In this study, Ni and transition metal (cobalt, iron, zinc, chromium, molybdenum, and tungsten) composites are fabricated using a simple electrodeposition and their HOR activity is evaluated. Based on the quick screening results, Ni-Mo is presented as a highly active HOR catalyst and characterized using transmission electron microscopy (TEM), X-ray photoelectron spectroscopy (XPS), X-ray diffraction (XRD), and energy-dispersive spectrometry (EDS) with various Mo compositions (Ni-xMo, x = 22, 24, 29, 33 wt%). The best-performing Ni-29Mo composite catalyst is artificially deactivated and compared to the pristine state to identify the key component for efficient HOR catalysis on Ni. Moreover, to understand synergetic effect between Ni and Mo species, DFT calculation was adopted to estimate hydrogen binding energy (HBE). To demonstrate applicability of the catalyst in a practical form, Ni-Mo nanoparticle catalyst was prepared and fabricated into membrane-electrode assembly for AEMFC test.

2. Experimental

2.1. Synthesis of nickel (Ni) and nickel-metal (Ni-M) film electrodes

Nickel and nickel-metal film electrodes were prepared through electrodeposition. A bath solution was composed of 0.1 M nickel chloride ($NiCl_2$) as a nickel precursor and 0.2 M trisodium citrate dihydrate as an additive. 0.01 or 0.03 M cobalt (II) chloride ($CoCl_2$), iron (II) chloride ($FeCl_2$), zinc (II) chloride ($ZnCl_2$), sodium chromate (VI) (Na_2CrO_4), sodium molybdate (VI) (Na_2MoO_4), and sodium tungstate (VI) (Na_2WO_4) were added to the bath solution to obtain Ni-M (M=Co, Fe, Zn, Cr, Mo, W) electrodes, respectively (Table S1). To find the optimal Mo composition, the bath solutions with 0.00125, 0.025, 0.01, and 0.02 M Na_2MoO_4 (Table S2) were additionally prepared. All chemicals were purchased from Junsei Chemical.

For electrodeposition, a conventional three-electrode cell was constructed with a silver/silver chloride (Ag/AgCl) reference electrode and a Pt mesh counter electrode. As a substrate, a copper (Cu) rotating disk electrode (RDE) polished with 2000 and 4000 grit abrasive paper and 0.3 μm diamond particles were utilized. In every bath solution, cathodic direct current (DC) of 50 mA/cm^2 was applied to the mirror-polished Cu RDE for 10 min using a potentiostat (Princeton Applied Research Versastat 4) at room temperature. During the electrodeposition, the electrode potential was gradually changed from approximately − 1.7 to − 1.4 $V_{Ag/AgCl}$ (Fig. S1) and the RDE was rotated with 3600 rpm to remove hydrogen bubbles from the electrode surface.

2.2. Synthesis of Ni-Mo nanoparticles

Ni-Mo nanoparticles were synthesized through a chemical reduction and heat treatment. 1.5 g of nickel nitrate hexahydrate (Junsei) and 0.63 g of sodium molybdate dihydrate (Junsei) were dissolved in 10 mL of deionized (DI) water with 5 mL of 25 wt% ammonium hydroxide solution (Junsei). Then, 50 mL of diethylene glycol (Junsei) was added

to the solution. The prepared solution was heated to 110 °C for three hours and then centrifuged with 5000 rpm. The collected powder was rinsed using DI water and acetone and dried overnight at 60 °C. The dried powder was grinded and heat-treated at 450 °C for 1 h under a 4% hydrogen (H_2) in argon (Ar) atmosphere [31]. Composition of the Ni-Mo nanoparticles are summarized in Table S3.

2.3. Materials characterization

The crystal structure and microstructure of the prepared catalysts were investigated using X-ray diffraction (XRD, Rigaku Ultima IV) and transmission electron microscopy (TEM, FEI Tecnai G2 F30 S-Twin). A focused ion beam (FEI, Helios Nanolab 450 F1) was used to prepare the TEM samples. The samples were examined using scanning electron microscopy (SEM, Philips XL 30) and their chemical compositions were measured using energy dispersive X-ray spectroscopy (EDX) equipped with SEM. The electronic structure of Ni and Mo was analyzed using X-ray photoelectron spectroscopy (XPS, Thermo VG Scientific Sigma Probe).

2.4. Measurement of electrochemical performance

Electrochemical performance was measured in a conventional three-electrode cell using a potentiostat (Princeton Applied Research Versastat 4). The Ni-M (M= Co, Fe, Zn, Cr, Mo, W) films as-electrodeposited on a Cu RDE were used as a working electrode. To evaluate performance of nanoparticle catalysts, 10 mg of Ni-Mo nanoparticles were dispersed in a solvent composed of 600 μL of IPA:DI= 1:1 solution, with 30 μL 5 wt% Nafion solution as a binder. 9.87 μL of the prepared ink was dropped on a glassy carbon RDE using a micropipette and dried under vacuum to prepare a Ni-Mo nanoparticle working electrode (catalyst loading of 800 μg$_{metal}$/cm^2). A mercury/mercury oxide (Hg/HgO) electrode was used as a reference electrode and a platinum wire as a counter electrode. All the potentials measured with respect to Hg/HgO reference electrode were converted into reversible hydrogen electrode (RHE) potential.

The electrocatalytic activity toward the hydrogen oxidation reaction (HOR) was evaluated in a H_2-saturated 0.1 M potassium hydroxide (KOH) solution with a rotating speed of 1600 rpm. To remove capacitive current, the steady state polarization method was employed; the potential was increased by 5 mV and held for 30 s for current measurement in a potential range from − 0.1–0.12 mV$_{RHE}$. During the measurement, solution temperature was kept constant at various temperatures in a range from 275 to 313 K using a water bath. For iR correction, ohmic resistance was measured from electrochemical impedance spectroscopy (EIS) outcomes. To evaluate stability of the Ni-Mo catalysts, potential cycling was conducted in the potential range from 0 to 0.2 V_{RHE} at a potential sweep rate of 100 mV/s and chronoampeometry was performed at a constant potential of 20 mV$_{RHE}$.

For reference, HOR activity of a Pt RDE (Pt(poly)), 20 wt% Pt/C (Premetek) and 30 wt% carbon-supported PtRu alloy catalyst (PtRu/C, atomic ratio of Pt to Ru = 1:1, Sigma-Aldrich) was measured under the same conditions as employed for the Ni-Mo catalysts. 5 mg of 20 wt% Pt/C or 30 wt% PtRu/C was dispersed in 600 μL of IPA:DI= 1:1 solution with 30 μL of 5 wt% Nafion solution as a binder. Then, 7.41 μL of the prepared Pt/C ink or 4.94 μL of the prepared PtRu/C ink was dropped on a glassy carbon RDE using a micropipette and dried under vacuum. The catalyst loading amount was 60 μg$_{metal}$/cm^2 for both Pt/C and PtRu/C electrodes.

2.5. Single cell performance

A membrane-electrode assembly (MEA) was prepared using Ni-Mo nanoparticles in the anode of anion exchange membrane fuel cell (AEMFC). As a hydroxide ion conductive solid polymer membrane and ionomer, Tokuyama A201 and Tokuyama AS-4 were employed, respectively. Anode loading of Ni-Mo nanoparticles was 1.0 mg/cm^2.
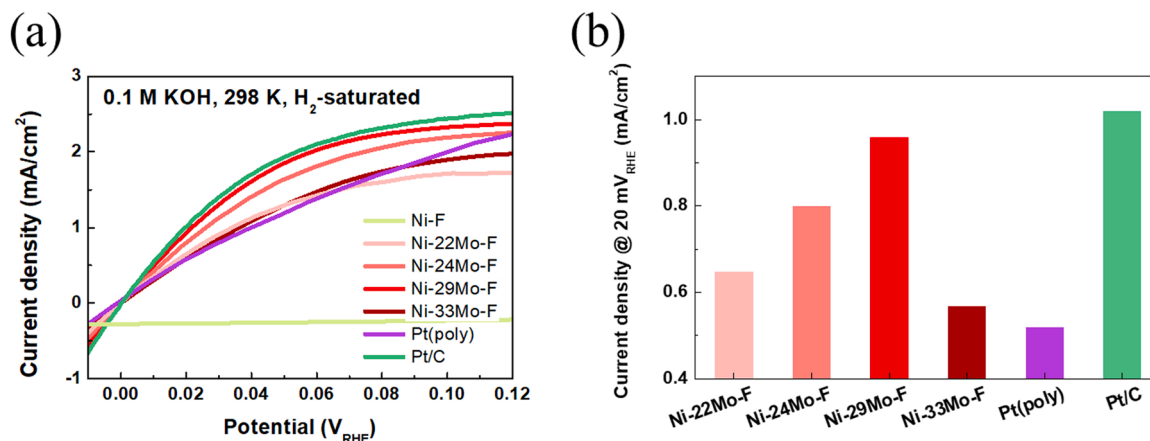
Fig. 1. (a) HOR polarization curves and (b) current density at 20 mV$_{RHE}$ for Ni and Ni-Mo films, Pt(poly), and Pt/C in a H$_2$-saturated 0.1 M KOH solution.

Cathode was prepared using commercial Pt/C (Tanaka 46.5 wt%) with Pt loading of 0.4 mg/cm^2. The Ni-Mo and Pt/C catalysts were spray-coated onto each side of a membrane, respectively. For the Ni-Mo anode, the ionomer content was changed from 10 to 30 wt% to examine effects of ionomer content on the fuel cell performance. For reference, a Pt/C (Tanaka 46.5 wt%) anode was fabricated with Pt loading of 1.0 mg/cm^2 with the Pt/C cathode. The electrode area was 5 cm^2. MEAs were assembled with gas diffusion layers (39 BCE, SGL carbon), Teflon gaskets, and graphite bipolar plates. Fully humidified hydrogen and oxygen were supplied to the anode and cathode, respectively, at a flow rate of 200 mL/min without back pressure. The cell temperature was kept at 65 °C.

3. Results and Discussion 3.1 Screening of Ni-M film catalysts

Ni and Ni-M (M= Co, Fe, Zn, Cr, Mo, W) catalysts were prepared through electrodeposition, to determine the element that enhances the electrocatalytic activity of Ni toward the hydrogen oxidation reaction (HOR). To evaluate the HOR activity, the Ni and Ni-M catalysts were prepared in a form of film on a Cu RDE (Fig. S2) so that the effects of surface area on the measured HOR current could be minimized. During electrodeposition of transition metals, hydrogen bubbles can be generated, producing a porous layer [32,33]. Under the condition employed in this study, relatively small cathodic overpotentials (Fig. S1) and the high rotating rate (3600 rpm) allowed formation of thin film layers (Fig. S3) rather than a porous structure. Table S1 and Fig. S4 summarize the chemical compositions of the prepared samples measured by energy dispersive X-ray spectroscopy (EDX). The Ni-to-(Ni+M) ratios were higher with 0.03 M metal precursor than with 0.01 M, for all elements. Although they showed variations due to the different reduction rates of each element, the Ni-to-(Ni+M) ratios were simply considered as high and low in this first quick screening step. Fig. S5(a) presents the HOR polarization curves of the Ni-M catalysts in a 0.1 M KOH solution. Among the prepared samples, the Ni-Mo catalysts exhibit the best HOR activity (Fig. S5(b)) and are investigated further in this study.

3.1. Characterization of Ni-Mo film catalysts

3.1.1. HOR activity and electrochemical properties of Ni-Mo film catalysts

To examine the effects of Mo content on the HOR activity of Ni-Mo film catalysts, various compositions of Ni-Mo film catalysts were prepared (Table S2 and Fig. S6). HOR polarization curves of the Ni and Ni-*x*Mo film catalysts (*x* = 22, 24, 29, and 33 at%) were measured (Fig. 1 (a)), in comparison to commercial Pt(poly), Pt/C and PtRu/C (Fig. S7). To minimize the capacitive current in the measured current, electrode potential was increased stepwise from − 0.1–0.12 V$_{RHE}$ by 5 mV with 30-second holding. The upper limit of potential sweep was determined as

0.12 V$_{RHE}$ to avoid oxidation of Ni [24]. Whereas Ni film (Ni-F) delivers negligible HOR current, Ni-Mo films exhibit significantly enhanced HOR activity, even higher than that of Pt(poly). Among the Ni-Mo films, Ni-29Mo-F catalyst shows the highest HOR current density at 20 mV$_{RHE}$ (0.96 mA/cm^2 @ 20 mV$_{RHE}$), which is 1.8 times higher than that of the Pt(poly) (0.52 mA/cm^2 @ 20 mV$_{RHE}$) and comparable to Pt/C (1.01 mA/cm^2 @ 20 mV$_{RHE}$). As reported in previous studies [18,34], PtRu/C shows remarkably higher HOR current density (Fig. S7, 2.01 mA/cm^2 @ 20 mV$_{RHE}$, iR-corrected) than Pt/C and Pt(poly), close to the Nernstian diffusion overpotential [15,16], making it difficult to obtain the kinetic current density for the HOR on PtRu/C [35]. Accordingly, Pt(poly) and Pt/C were selected as a reference catalyst in this study. With an increase or a decrease in Mo content from Ni-29Mo-F, HOR current was reduced. Micropolarization region (from −10 to 10 mV) was further examined to compare the intrinsic HOR activity of the prepared catalysts since effects of mass transport and ohmic resistance on the measured current are minimized in the overpotential region [36,37] (Fig. S8(a)). As a measure of intrinsic activity of a catalyst, polarization resistance (R$_p$) can be calculated from the following equations;

$$i = i_0 \left(e^{\frac{aF}{RT}\eta} - e^{\frac{(1-a)F}{RT}\eta} \right) \approx i_{0,micro}\frac{F}{RT}\eta \qquad (1)$$

$$\frac{\eta}{i} = \frac{RT}{i_{0,micro}F} = R_p \qquad (2)$$

where *i* is the measured current, *i$_o$* is exchange current density, α is charge transfer coefficient, F is Faraday constant, R is gas constant, T is temperature, and η is overpotential. As shown in Fig. S8(b), Ni-29Mo-F shows the smallest R$_p$ (12.2 Ω·cm^2) among the Ni-Mo films, which is even smaller than that of Pt(poly) (27.1 Ω·cm^2) and similar to that of Pt/C (10.5 Ω·cm^2). These results demonstrate that addition of Mo to Ni significantly improves the catalytic activity of Ni toward HOR and Ni-29Mo shows the best HOR activity, outperforming Pt.

To understand the HOR kinetics on Ni-29Mo-F, Pt(poly) and Pt/C, Tafel plots were collected at various temperatures in the range from 275 to 313 K (Fig. S9). For iR-correction, Nyquist plots were also obtained (Fig. S10). Using the Butler-Volmer equation (Eq. [2] in Supporting Information), exchange current density (i$_o$) were calculated (Fig. S11) and found to be 2.71 mA/cm^2 for Ni-29Mo-F at 298 K, which is higher than that of Pt(poly) (1.01 mA/cm^2) and comparable to that of Pt/C (3.01 mA/cm^2). These results reflect that the HOR kinetics is faster on Ni-29Mo than on Pt. From the exchange current densities, Arrhenius plots (log i$_0$ vs. 1/T) are illustrated in Fig. S12. The activation energy of the HOR on Ni-29Mo-F catalyst was measured as 31.0 kJ/mol, which is comparable to those on Pt(poly) (29.8 kJ/mol) and Pt/C (29.2 kJ/mol) Compared to Pt(poly), Ni-29Mo-F exhibits the faster HOR kinetics with similar activation energy, reflecting that Ni-29Mo-F has the higher
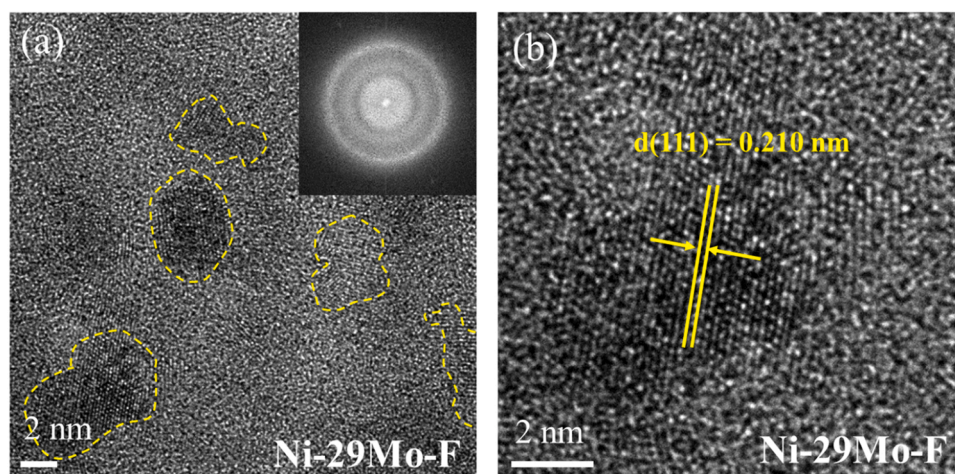
Fig. 2. TEM and FFT images of (a) Ni-29Mo-F and (b) magnified image of Ni-29Mo-F.

number of catalytically-active sites per unit area. As a measure of the catalytically-active sites, electrochemical surface areas (ECSAs) were estimated based on the hydrogen underpotential deposition current (Fig. S13(a)) and α-Ni(OH)$_2$ reduction current (Fig. S13(b)) [38,39] for Pt(poly) and Ni-29Mo-F, respectively. ECSA of Pt(poly) and Ni-29Mo-F were found to be 0.33 cm_{Pt}^2 and 15.4 cm_{Ni}^2, respectively. Accordingly, specific exchange current density defined as the exchange current density divided by ECSA was calculated to be 0.60 mA/cm_{Pt}^2 for Pt(poly), and 0.035 mA/cm_{Ni}^2 for Ni-29Mo-F at 298 K, supporting that Ni-29Mo-F has more catalytically-active sites than Pt(poly).

To obtain the number of electrons (n) involved in the HOR on Ni-29Mo-F and Pt/C, the HOR current was measured at various rotation speeds [40] (Figs. S14(a) and (c)). From the slope of Koutecký-Levich plots (Figs. S14(b) and (d)) [40,41], n was calculated and found to be 1.96 and 2.02 for Ni-29Mo-F and Pt/C, respectively, implying that 2-electron hydrogen oxidation reaction occurs on Ni-29Mo-F and Pt/C without producing byproducts. In addition, the linear polarization curves of Ni-29Mo-F collected in an Ar-saturated 0.1 M KOH solution (Fig. S15(a)) show negligible anodic current at potentials more positive than 0 V_{RHE}. These results imply that the anodic current of Ni-29Mo-F measured in a H$_2$-saturated KOH solution is related to the hydrogen oxidation reaction.

Stability of Ni-29Mo-F and Pt/C were estimated by conducting potential cycling and chronoamperometry. Before and after 2000 potential cycles from 0 to 0.2 V_{RHE} [26,42], HOR polarization curves were measured (Fig. S16(a), (b)), revealing negligible changes in the HOR current both on Ni-29Mo-F and Pt/C. In addition, current density measured at a constant applied potential of 20 mV_{RHE} (Fig. S16(c)) was slightly reduced by 0.04 mA/cm^2 and 0.03 mA/cm^2 for Ni-29Mo-F and Pt/C, respectively, for 5 h. These results demonstrate Ni-29Mo-F is as stable as Pt/C under the alkaline condition.

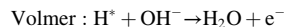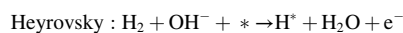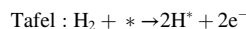### 3.1.2. Microstructure of Ni-Mo film catalysts

To explore the factors that determine the HOR activity of Ni-Mo-F, structural features were examined. XRD patterns of the Ni-Mo-F samples (Fig. S17) present only Cu substrate peaks, reflecting that the Ni-Mo-F samples have an amorphous structure or very low crystallinity [43]. TEM images of Ni-22Mo-F, Ni-29Mo-F, and Ni-33Mo-F were collected in comparison with Ni-F (Fig. 2, Fig. S18). Fast Fourier transform (FFT) patterns of the Ni-Mo-F samples present blurred rings, indicating a highly amorphous structure (inset of Fig. 2(a), Figs. S18(a), (c)). However, nanometer-sized crystallites are observed in the samples, particularly in Ni-29Mo-F, as marked by yellow dashed lines in Fig. 2(a) and Fig. S19. Fig. 2(b) shows the crystallite in Ni-29Mo-F have D-spacing of 0.210 nm, which is slightly larger than that of Ni(111) planes (0.204 nm, Fig. S18(f)). Ni(111) is known as the most stable surface of

Ni [44]. Considering the atomic radius of Mo (0.145 nm) and Ni (0.135 nm), the slight increase in the Ni(111) lattice parameter reflects that the Ni(111) crystallites in Ni-29Mo-F are alloyed with Mo. Metallic Ni is known to be more active toward HOR than oxidized Ni [25,45]. Thus, the Ni(111) crystallites could be related to the HOR activity of Ni-Mo-F. Although Ni-F illustrates higher crystallinity than Ni-Mo films (Figs. S18(e) and (f)), it has negligible catalytic activity toward HOR. These outcomes demonstrate that not only Ni(111) crystallites but also Mo species are necessary in achieving high HOR activity.

3.1.3. Oxidation state of Ni and Mo in Ni-Mo film catalysts

The catalytic activity of Ni-based catalysts is highly affected by the oxidation state of Ni [27,46]. Fig. 3(a) shows the Ni 2p XPS spectra of Ni-Mo film catalysts, which were deconvoluted into Ni (852.3 eV), Ni (OH)$_2$ (855.8 eV), and NiO(853.6 eV) [47–51]. By calculating the area of those peaks, the compositions of Ni(0) and Ni^{2+} (Ni(OH)$_2$ and NiO) were obtained, as presented in Fig. 3(b). Among the prepared samples, Ni-29Mo-F has the highest Ni(0) composition, 48.4%. With increasing or decreasing Mo content from Ni-29Mo, Ni(0) composition is lowered. Interestingly, a higher Ni(0) to Ni^{2+} ratio can be correlated with higher HOR activity, indicating that metallic Ni contribute to the HOR activity. However, the similar Ni(0) to Ni^{2+} ratios of Ni-F and Ni-29Mo-F show that metallic Ni is not the only factor to determine the HOR activity and Mo species are necessary to enhance the HOR activity.

It has been reported that metallic Ni plays key roles in the HOR on Ni-based catalysts [21,46,52] by serving as a hydrogen adsorption site.

Tafel : $H_2 + * \rightarrow 2H^* + 2e^-$

Heyrovsky : $H_2 + OH^- + * \rightarrow H^* + H_2O + e^-$

Volmer : $H^* + OH^- \rightarrow H_2O + e^-$

where H* indicates surface adsorbed hydrogen. By connecting these previous reports to the HOR catalytic activity of Ni-Mo film catalysts, it would be reasonable to consider that a greater amount of metallic Ni can enhance the HOR activity of the Ni-Mo film by increasing hydrogen adsorption sites, which is most efficiently created in Ni-29Mo-F.

Mo 3d XPS spectra of Ni-Mo-F samples show Mo(0) (277.8 eV), Mo^{4+}(229.1 eV), Mo^{5+}(230.4 eV) and Mo^{6+}(232.0 eV) species [53] (Fig. 3(c)). Mo(0) composition was highest in Ni-29Mo-F and lowered with increasing or decreasing Mo content in Ni-Mo-F samples, implying that Mo was alloyed with the Ni(111) crystallites in metallic state. Compositions of oxidized Ni and Mo are more than 50% and 70%, respectively (Fig. 3(b) and (d)). All these outcomes imply that Ni-Mo films are composed of nanometer-sized Ni-rich crystallites and
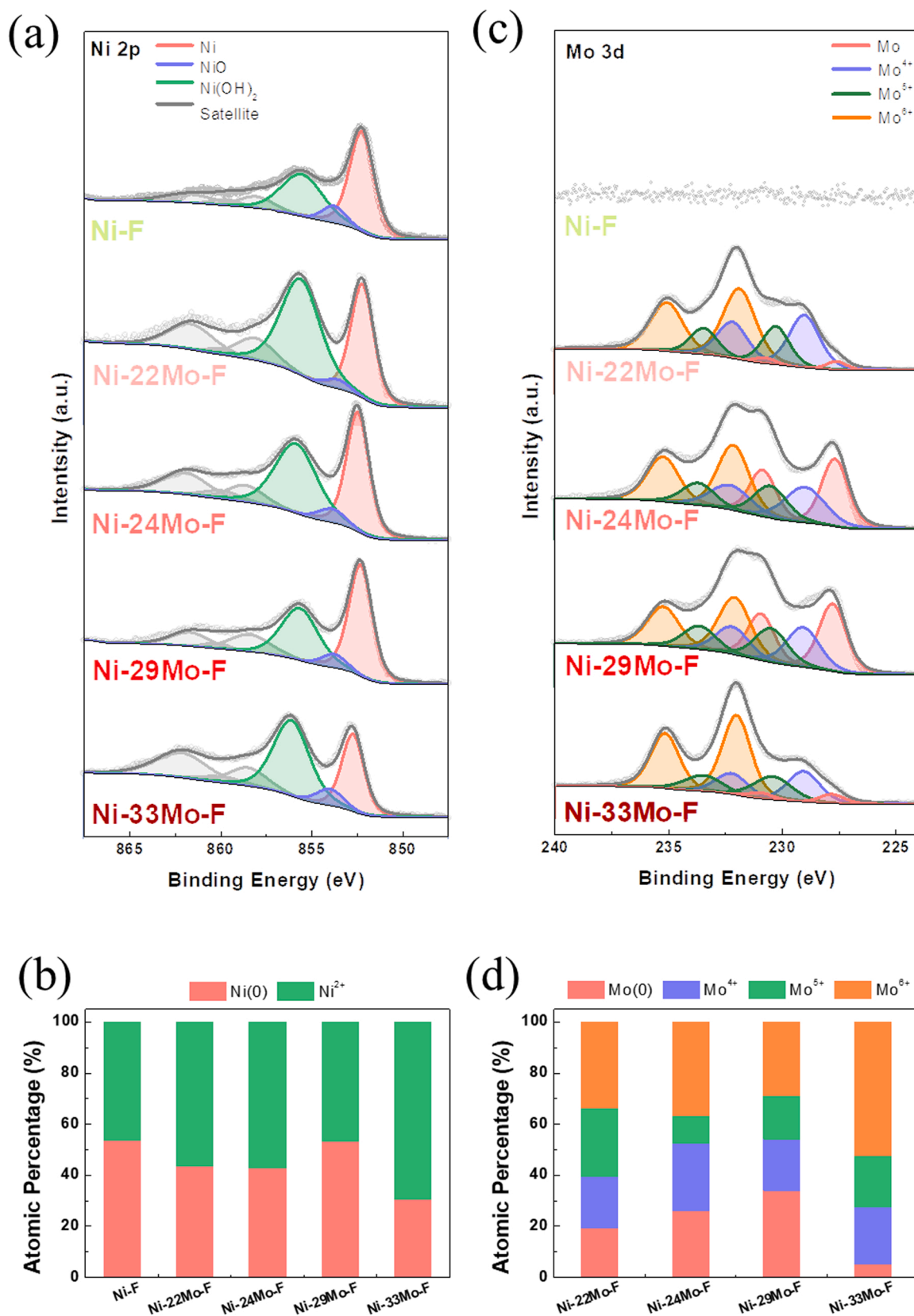
Fig. 3. (a) Ni 2p XPS spectra, (b) atomic percentage of Ni oxidation state, (c) Mo 3d XPS spectra and (d) atomic percentage of Mo oxidation state in Ni-Mo film catalysts.
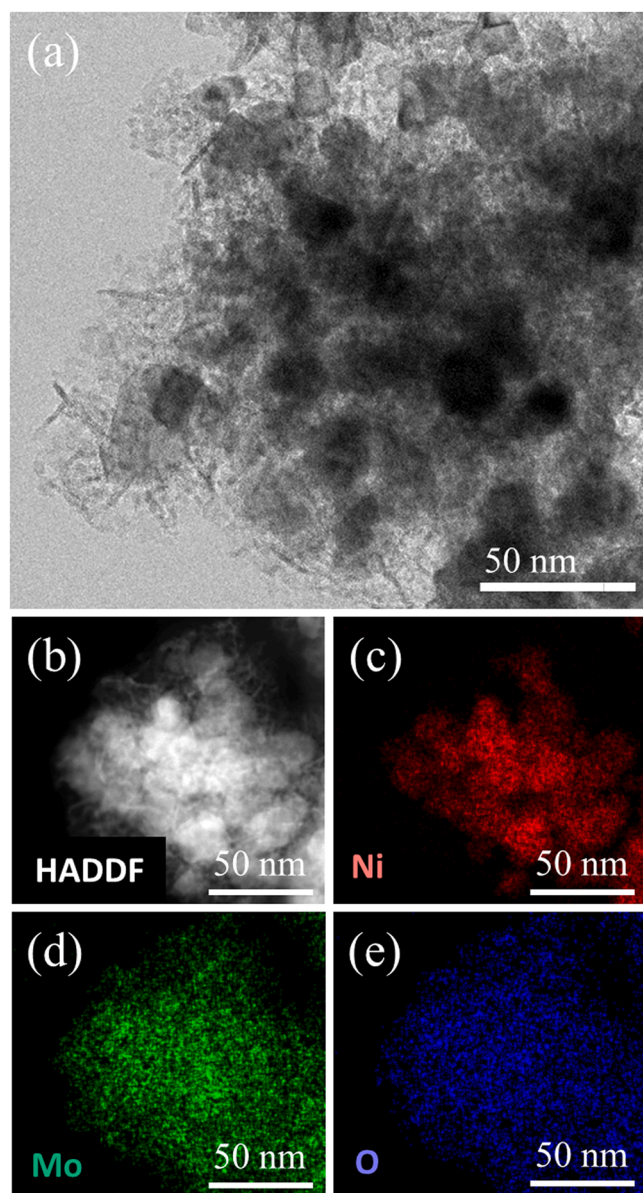
Fig. 4. (a) Bright field and (b) HAADF TEM images of Ni-29Mo-NP and corresponding elemental mapping images for (c) nickel (d) molybdenum and (e) oxygen.

amorphous $NiMoO_x$ and the HOR activity is related to the compositions of metallic Ni and Mo in Ni-Mo-F.

3.2. Ni-Mo nanoparticle characterization

3.2.1. Microstructure analysis of Ni-Mo nanoparticles

To apply the Ni-Mo catalyst in the anode of anion exchange membrane fuel cell (AEMFC), Ni-29Mo nanoparticles were synthesized. To confirm the effects of Mo content on the HOR activity, Ni-20Mo, Ni-25Mo, and Ni-33Mo nanoparticles (NP) were also prepared (Table S3). XRD patterns of Ni-Mo-NP samples (Fig. S20) clearly demonstrate the diffraction peaks corresponding to metallic Ni with small amount of NiO. In addition, with an increase in Mo content, the (111) peak was negatively shifted, implying that Mo was alloyed in the metallic Ni phase. Using the Bragg's law and the 2θ (44.14°) of NiMo(111), lattice parameter of Ni-29Mo-NP was calculated and found to be 0.205 nm. The crystallite size was measured using the Scherrer equation, giving a value of 14 nm. TEM image of Ni-29Mo-NP (Fig. 4) shows particle sizes of approximately several tens of nanometers. High magnification TEM image (Fig. S21) displays crystallites corresponding Ni(111) with the D-spacing of 0.205 nm, in accordance with the XRD outcomes. These results support that Mo is alloyed in the Ni(111) structure. The smaller lattice parameter of Ni-29Mo-NP compared to that of Ni-29Mo-F might be associated with the small particle sizes. Previous reports have found that smaller particle size can lead to a reduced lattice parameter [54,55]. Elemental line scanning (Fig. S22) and EDX mapping images (Fig. 4 (c)-(e)) demonstrate that the Ni-Mo nanoparticles are composed of Ni-rich metallic phase and Mo-rich oxide phase.

3.2.2. HOR activity of Ni-Mo nanoparticles

Fig. 5(a) shows HOR polarization curves of Ni-Mo NP catalysts. In accordance with the film catalysts, Ni-29Mo-NP showed the highest HOR current density (1.12 mA/cm^2 at 20 mV$_{RHE}$ (Fig. 5(b)), which is about 9% higher than Pt/C (1.01 mA/cm^2) and 17% higher than Ni-29Mo-F (0.96 mA/cm^2). With increasing or decreasing Mo content, HOR activity was lowered. Catalytic activity of Ni-29Mo-NP shows a high record among the previously-reported non-PGM HOR catalysts, as summarized in Table S5. The number of electrons involved in HOR was also measured from rotation test as shown in Figs. S14(e) and (f) and found to be 2.04. Similar to Ni-29Mo-F (Fig. S15(a)), the anodic current of Ni-29Mo-NP collected at potentials positive than 0 V$_{RHE}$ in a H$_2$-saturated 0.1 M KOH solution can be attributed to HOR since Ni-29Mo-NP reveals negligible anodic current in the same potential region in an Ar-saturated solution (Fig. S15(b)).

After conducting 2000 potential cycles from 0 to 0.2 V$_{RHE}$ (Fig. S23 (a), (b)), HOR polarization curves of Ni-29Mo-NP and Pt/C display negligible changes in the current, reflecting Ni-29Mo-NP and Pt/C have similar stability under the alkaline HOR condition. Chronoamperometry
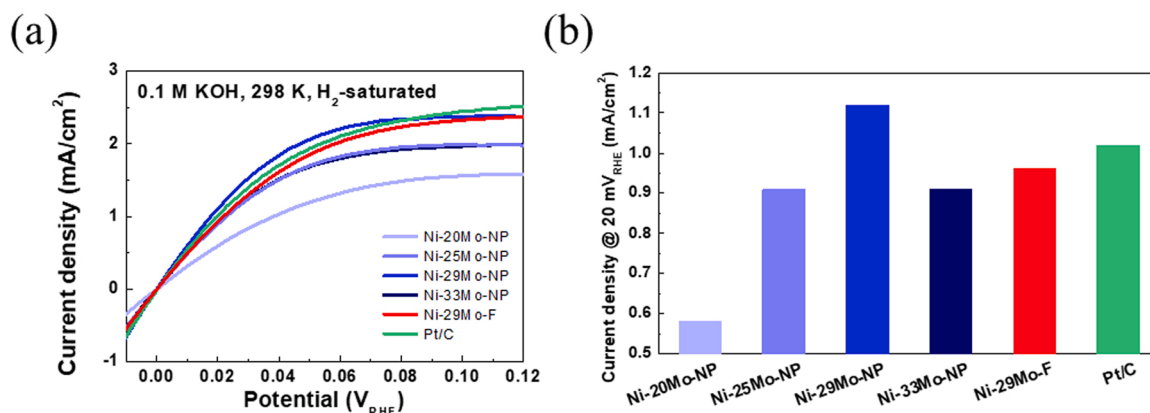

Fig. 5. (a) HOR polarization curves and (b) current density at 20 mV$_{RHE}$ of Ni-Mo nanoparticles and Pt/C in a H$_2$-saturated 0.1 M KOH solution.
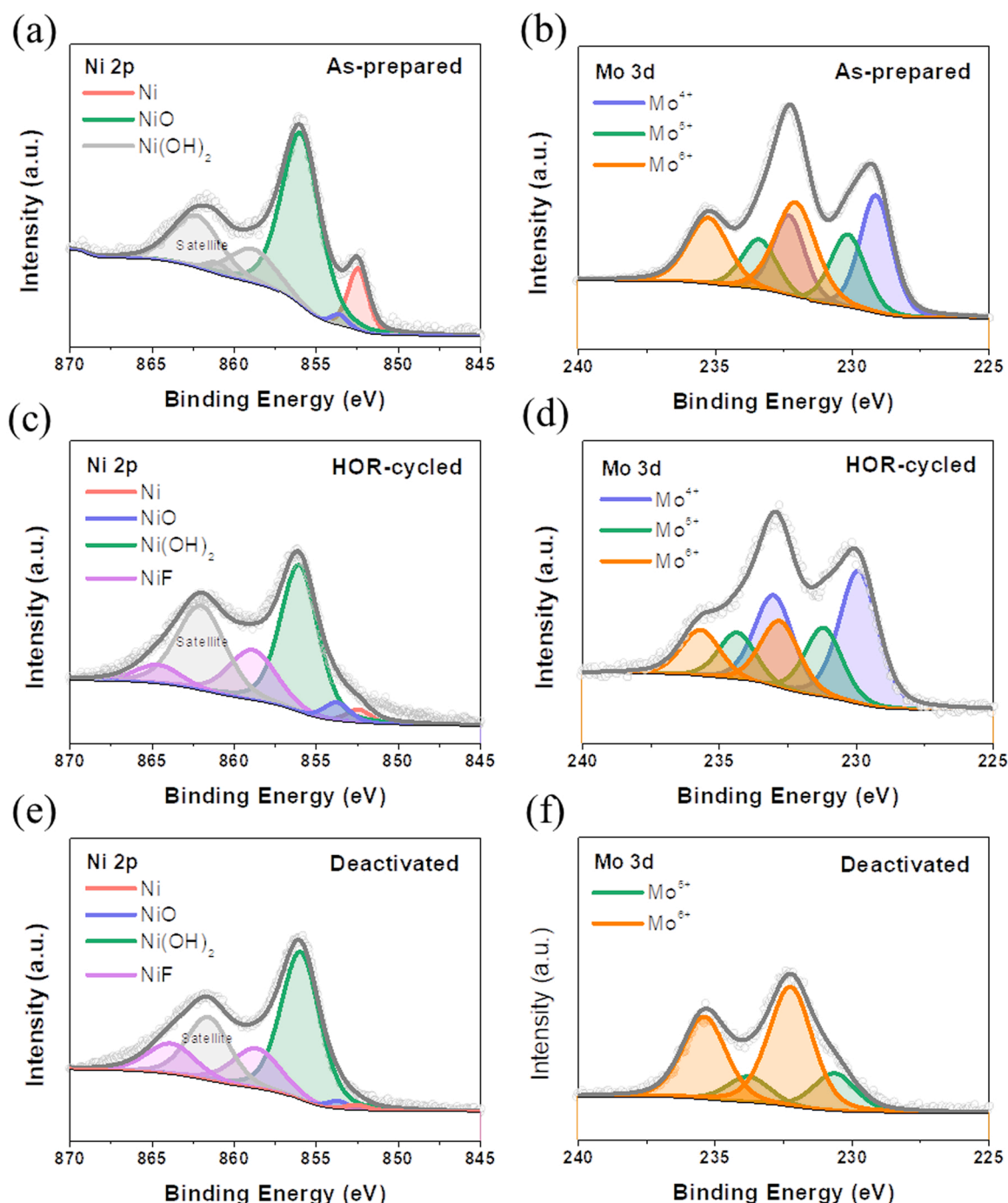
Fig. 6. Ni 2p and Mo 3d XPS spectra of (a), (b) as-prepared Ni-29Mo-NP, (c), (d) HOR-cycled Ni-29Mo-NP, and (e), (f) of deactivated Ni-29Mo-NP, respectively.

results obtained at 20 mV$_{RHE}$ for 5 h (Fig. S23(c)) also support superior stability of Ni-29Mo-NP similar to Pt/C (Fig. S16).

To identify the HOR activity-determining factor, Ni-29Mo-NP was deactivated (refer to supplementary information for detailed preparation method, Fig. S24). By simply immersing the sample in a 0.1 M KOH solution, the HOR activity of Ni-29Mo-NP was almost completely lost. Fig. 6 presents Ni 2p and Mo 3d XPS spectra of as-prepared, HOR-cycled and deactivated Ni-29Mo-NP. As-prepared sample exhibits 21.6% metallic Ni and 78.4% oxidized Ni. Ni-29Mo-NP shows the higher composition of oxidized Ni compared to Ni-29Mo-F (53.3%), possibly due to the higher surface-to-bulk ratio of the nanoparticles. In both the HOR-cycled and deactivated samples, metallic Ni peak was significantly diminished, owing to the oxidation of Ni in the alkaline solution and

exposure to air for the ex-situ XPS analysis [56]. It should be noted that the deactivated Ni-29Mo-NP is composed of Mo^{5+} and Mo^{6+} without Mo^{4+} whereas the as-prepared and HOR-cycled sample display significant Mo^{4+} peak. These outcomes demonstrate that Mo^{4+} or MoO$_2$ species is necessary for the HOR.

3.2.3. Anion exchange membrane fuel cell (AEMFC) performance

Single cell test was performed to validate applicability of Ni-29Mo-NP nanoparticle as a convincing catalyst for AEMFC anode. Firstly, ionomer content in anode catalyst layer was varied to optimize MEA fabrication condition and 15 wt% of ionomer content showed highest performance (Fig. S25). Fig. 7 shows single cell performance employing Ni-29Mo-NP and Pt/C as an anode catalyst. Maximum power density of
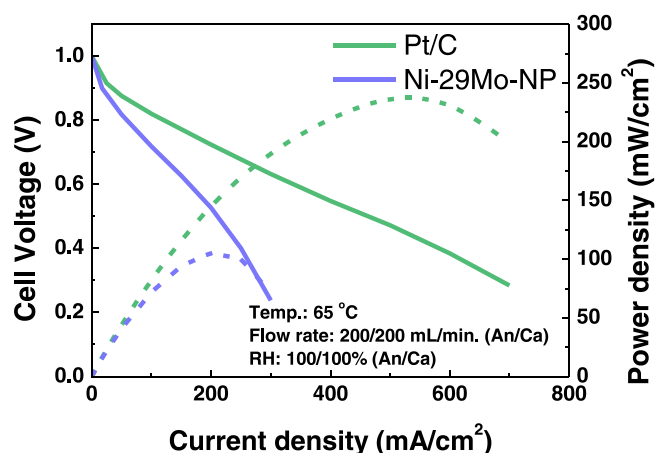
Fig. 7. Anion exchange membrane fuel cell performance of Ni-29Mo-NP and Pt/C anode with Pt/C cathode.

Pt/C anode was 234 mW/cm^2 at a current density of 500 mA/cm^2. Ni-29Mo-NP anode showed maximum power density of 105 mW/cm^2 at a current density of 200 mA/cm^2. The maximum power density of Ni-29Mo-NP anode is about half of that of Pt/C anode. To the best of our knowledge, only a few reports demonstrate AEMFC performance using non-precious anode catalyst and the single cell performance of Ni-29Mo-NP is of the highest level, which were also summarized in Table S4. These results show the Ni-Mo nanoparticles are a promising non-precious catalyst for AEMFC.

3.2.4. DFT calculation of Ni-Mo catalyst

As described above, metallic Ni serves as a hydrogen adsorption site and MoO$_2$ species is necessary for the HOR. To understand the superior HOR activity of Ni-29Mo, HBE was examined using DFT calculation (for further computational details, refer to Supplementary Information). Although the structural analyses demonstrated that Ni-29Mo-NP is composed of Ni-rich (111) crystallites and Mo-rich oxide (Fig. 4 and Fig. S13), a model structure was established based on metallic Ni(111) and MoO$_x$ phase (Fig. 8(a)).

The HBE of Ni(111) was calculated as − 0.42 eV (Fig. 8(b)), which is stronger than that of Pt(111) by about − 0.35 eV. As mentioned above, the strong HBE of Ni can lower the HOR activity by suppressing the Volmer reaction. On the other hand, MoO$_2$ shows a positive HBE, about 1.92 eV, reflecting that hydrogen is hardly adsorbed on the surface of MoO$_2$. Thus, MoO$_2$ might not be an active site for the HOR. However, the positive HBE of MoO$_2$ can shift the neighboring Ni's HBE to a weaker value, resulting in an improvement of HOR activity. A previous study of Jiang et al. [57] suggested that a combination of Ru with strong HBE and MoO$_2$ with a positive HBE could achieve an HBE close to 0 eV, which is an ideal value for the hydrogen reaction. Similarly, interaction between

Ni with a strong HBE and MoO$_2$ in the Ni-Mo catalyst also can result in enhancement of the HOR activity by achieving the ideal HBE on the surface of Ni of the Ni-Mo catalyst. Thus, Ni-29Mo can exhibit the highest HOR activity represented as high exchange current density and comparable activation energy to Pt/C, while pure Ni showed negligible HOR activity (Fig. 1(a)).

4. Conclusions

Ni-M (Co, Fe, Zn, Cr, Mo, W) alloy catalysts were screened using electrodeposition. Among the prepared samples, Ni-29Mo exhibited the best HOR activity. The Ni-29Mo film showed superior HOR activity (0.96 mA/cm^2 @ 20 mV$_{RHE}$), that is higher than Pt(poly) (0.52 mA/cm^2 @ 20 mV$_{RHE}$) and comparable to that of Pt/C catalyst (1.01 mA/cm^2 @ 20 mV$_{RHE}$). The HOR activity shows a correlation with metallic Ni-to-oxidized Ni and with metallic Mo-to-oxidized Mo ration in Ni-Mo film catalysts with various Mo content, which was found from XPS result. Higher metallic Ni content can lead to higher HOR activity, since metallic Ni site act as active site. Ni-Mo nanoparticles, which was constructed with Ni embedded MoO$_x$ matrix structure, were synthesized to be fabricated into a membrane-electrode assembly (MEA) for anion exchange membrane fuel cell (AEMFC). Ni-29Mo-NP showed an excellent HOR current (1.12 mA/cm^2 @ 20 mV$_{RHE}$), which was 12% higher than a commercial Pt/C catalyst. The AEMFC assembled with the Ni-29Mo anode showed power density of 105 mW/cm^2, which was about half of the performance of counterpart Pt/C anode cell (234 mW/cm^2). These results indicate its strong applicability as an anode catalyst for AEMFC application. Through a deactivation test of Ni-Mo nanoparticles, MoO$_2$ was identified to have a key role for enhancing the HOR activity of Ni and DFT calculations revealed that the low HBE of MoO$_2$ might lower the HBE of Ni, which in turn could increase the HOR catalytic activity of Ni.

CRediT authorship contribution statement

YongKeun Kwon: Conceptualization, Methodology, Validation, Formal analysis, Investigation, Writing – Original Draft, Writing – Review & Editing, Visualization. **Doosun Hong**: Methodology, Software, Formal analysis. **Jue-Hyuk Jang**: Methodology, Validation, Investigation. **MinJoong Kim**: Validation, Formal anlaysis. **SeKwon Oh**: Validation, Formal anlaysis. **DongHoon Song**: Validation, Investigation. **JeongHoon Lim**: Validation, Investigation. **Sung Jong Yoo**: Writing – Review & Editing, Supervision, Project administration. **EunAe Cho**: Conceptualization, Writing – Review & Editing, Supervision, Project administration.

Declaration of Competing Interest

The authors declare that they have no known competing financial interests or personal relationships that could have appeared to influence
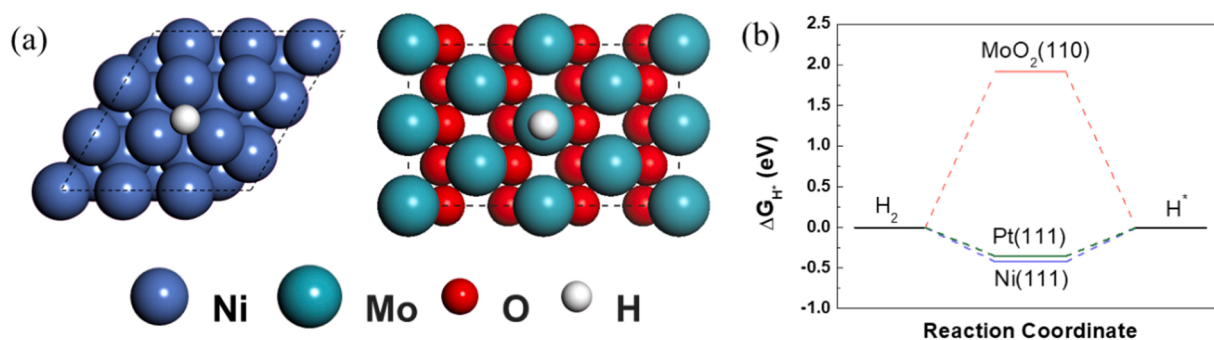

Fig. 8. (a) Top view of Ni(111) (left) and MoO$_2$ (right) (Green: Ni, Cyan: Mo, Red: O, White: H) and (b) hydrogen adsorption energy (ΔG_{H^*}) on Ni(111), Pt(111), and MoO$_2$(110).

the work reported in this paper.

Data Availability

Data will be made available on request.

Acknowledgements

Appendix A. Supporting information

Supplementary data associated with this article can be found in the online version at doi:10.1016/j.apcatb.2023.122740.

References

[1] H.A. Gasteiger, N.M. Marković, Just a dream—or future reality? science 324 (2009) 48–49.

[2] A. Holewinski, J.-C. Idrobo, S. Linic, High-performance Ag–Co alloy catalysts for electrochemical oxygen reduction, Nat. Chem. 6 (2014) 828.

[3] M. Liu, Z. Zhao, X. Duan, Y. Huang, Nanoscale structure design for high-performance pt-based ORR catalysts, Adv. Mater. 31 (2019) 1802234.

[4] S. Sui, X. Wang, X. Zhou, Y. Su, S. Riffat, C.-J. Liu, A comprehensive review of Pt electrocatalysts for the oxygen reduction reaction: Nanostructure, activity, mechanism and carbon support in PEM fuel cells, J. Mater. Chem. A 5 (2017) 1808–1825.

[5] C. Wang, N.M. Markovic, V.R. Stamenkovic, Advanced platinum alloy electrocatalysts for the oxygen reduction reaction, Acs Catal. 2 (2012) 891–898.

[6] A. Freund, J. Lang, T. Lehmann, K.A. Starz, Improved Pt alloy catalysts for fuel cells, Catal. Today 27 (1996) 279–283.

[7] X. Wan, X. Liu, Y. Li, R. Yu, L. Zheng, W. Yan, H. Wang, M. Xu, J. Shui, Fe–N–C electrocatalyst with dense active sites and efficient mass transport for high-performance proton exchange membrane fuel cells, Nat. Catal. 2 (2019) 259.

[8] S. Chen, H.A. Gasteiger, K. Hayakawa, T. Tada, Y. Shao-Horn, Platinum-alloy cathode catalyst degradation in proton exchange membrane fuel cells: nanometer-scale compositional and morphological changes, J. Electrochem. Soc. 157 (2010) A82–A97.

[9] A. Kongkanand, M.F. Mathias, The priority and challenge of high-power performance of low-platinum proton-exchange membrane fuel cells, J. Phys. Chem. Lett. 7 (2016) 1127–1137.

[10] S. Ratso, N.R. Sahraie, M.T. Sougrati, M. Käärik, M. Kook, R. Saar, P. Paiste, Q. Jia, J. Leis, S. Mukerjee, Synthesis of highly-active Fe–N–C catalysts for PEMFC with carbide-derived carbons, J. Mater. Chem. A 6 (2018) 14663–14674.

[11] S. Brocato, A. Serov, P. Atanassov, pH dependence of catalytic activity for ORR of the non-PGM catalyst derived from heat-treated Fe–phenanthroline, Electrochim. Acta 87 (2013) 361–365.

[12] M. Piana, S. Catanorchi, H. Gasteiger, Kinetics of non-platinum group metal catalysts for the oxygen reduction reaction in alkaline medium, ECS Trans. 16 (2008) 2045–2055.

[13] D.R. Dekel, Review of cell performance in anion exchange membrane fuel cells, J. Power Sources 375 (2018) 158–169.

[14] J.R. Varcoe, P. Atanassov, D.R. Dekel, A.M. Herring, M.A. Hickner, P.A. Kohl, A. R. Kucernak, W.E. Mustain, K. Nijmeijer, K. Scott, Anion-exchange membranes in electrochemical energy systems, Energy Environ. Sci. 7 (2014) 3135–3191.

[15] D. Strmcnik, M. Uchimura, C. Wang, R. Subbaraman, N. Danilovic, D. van der Vliet, A.P. Paulikas, V.R. Stamenkovic, N.M. Markovic, Improving the hydrogen oxidation reaction rate by promotion of hydroxyl adsorption, Nat. Chem. 5 (2013) 300–306.

[16] W. Sheng, H.A. Gasteiger, Y. Shao-Horn, Hydrogen oxidation and evolution reaction kinetics on platinum: acid vs alkaline electrolytes, J. Electrochem. Soc. 157 (2010) B1529–B1536.

[17] N. Maiorova, A. Mikhailova, O. Khazova, V. Grinberg, Thin-film rotating disk electrode as a tool for comparing the activity of catalysts in the hydrogen oxidation reaction, Russ. J. Electrochem. 42 (2006) 331–338.

[18] Y. Wang, G. Wang, G. Li, B. Huang, J. Pan, Q. Liu, J. Han, L. Xiao, J. Lu, L. Zhuang, Pt–Ru catalyzed hydrogen oxidation in alkaline media: Oxophilic effect or electronic effect? Energy Environ. Sci. 8 (2015) 177–181.

[19] I. Matanovic, H.T. Chung, Y.S. Kim, Benzene adsorption: a significant inhibitor for the hydrogen oxidation reaction in alkaline conditions, J. Phys. Chem. Lett. 8 (2017) 4918–4924.

[20] T. Tomida, I. Nakabayashi, Spongy Raney nickel hydrogen electrodes for alkaline fuel cells, J. Electrochem. Soc. 136 (1989) 3296–3298.

[21] J. Linnekoski, A. Krause, J. Keskinen, J. Lamminen, T. Anttila, Processing of Raney-nickel catalysts for alkaline fuel cell applications, J. fuel Cell Sci. Technol. 4 (2007) 45–48.

[22] P. Quaino, F. Juarez, E. Santos, W. Schmickler, Volcano plots in hydrogen electrocatalysis–uses and abuses, Beilstein J. Nanotechnol. 5 (2014) 846–854.

[23] Z.W. Seh, J. Kibsgaard, C.F. Dickens, I. Chorkendorff, J.K. Nørskov, T.F. Jaramillo, Combining theory and experiment in electrocatalysis: Insights into materials design, Science 355 (2017).

[24] W. Sheng, A.P. Bivens, M. Myint, Z. Zhuang, R.V. Forest, Q. Fang, J.G. Chen, Y. Yan, Non-precious metal electrocatalysts with high activity for hydrogen oxidation reaction in alkaline electrolytes, Energy Environ. Sci. 7 (2014) 1719–1724.

[25] Z. Zhuang, S.A. Giles, J. Zheng, G.R. Jenness, S. Caratzoulas, D.G. Vlachos, Y. Yan, Nickel supported on nitrogen-doped carbon nanotubes as hydrogen oxidation reaction catalyst in alkaline electrolyte, Nat. Commun. 7 (2016) 10141.

[26] Y. Duan, Z.-Y. Yu, L. Yang, L.-R. Zheng, C.-T. Zhang, X.-T. Yang, F.-Y. Gao, X.-L. Zhang, X. Yu, R. Liu, Bimetallic nickel-molybdenum/tungsten nanoalloys for high-efficiency hydrogen oxidation catalysis in alkaline electrolytes, Nat. Commun. 11 (2020) 1–10.

[27] Y. Yang, X. Sun, G. Han, X. Liu, X. Zhang, Y. Sun, M. Zhang, Z. Cao, Y. Sun, Enhanced electrocatalytic hydrogen oxidation on ni/nio/c derived from a nickel-based metal–organic framework, Angew. Chem. 131 (2019) 10754–10759.

[28] O.V. Cherstiouk, P.A. Simonov, A.G. Oshchepkov, V.I. Zaikovskii, T.Y. Kardash, A. Bonnefont, V.N. Parmon, E.R. Savinova, Electrocatalysis of the hydrogen oxidation reaction on carbon-supported bimetallic NiCu particles prepared by an improved wet chemical synthesis, J. Electroanal. Chem. 783 (2016) 146–151.

[29] J. Fan, M. Chen, Z. Zhao, Z. Zhang, S. Ye, S. Xu, H. Wang, H. Li, Bridging the gap between highly active oxygen reduction reaction catalysts and effective catalyst layers for proton exchange membrane fuel cells, Nature, Energy 6 (2021) 475–486.

[30] A. Roy, M.R. Talarposhti, S.J. Normile, I.V. Zenyuk, V. De Andrade, K. Artyushkova, A. Serov, P. Atanassov, Nickel–copper supported on a carbon black hydrogen oxidation catalyst integrated into an anion-exchange membrane fuel cell, Sustainable, Energy Fuels 2 (2018) 2268–2275.

[31] J.R. McKone, B.F. Sadtler, C.A. Werlang, N.S. Lewis, H.B. Gray, Ni–Mo nanopowders for efficient electrochemical hydrogen evolution, ACS Catal. 3 (2013) 166–169.

[32] D. Song, D. Hong, Y. Kwon, H. Kim, J. Shin, H.M. Lee, E. Cho, Highly porous Ni–P electrode synthesized by an ultrafast electrodeposition process for efficient overall water electrolysis, J. Mater. Chem. A 8 (2020) 12069–12079.

[33] S. Oh, H. Kim, Y. Kwon, M. Kim, E. Cho, H. Kwon, Porous Co–P foam as an efficient bifunctional electrocatalyst for hydrogen and oxygen evolution reactions, J. Mater. Chem. A 4 (2016) 18272–18277.

[34] Y. Cong, B. Yi, Y. Song, Hydrogen oxidation reaction in alkaline media: From mechanism to recent electrocatalysts, Nano Energy 44 (2018) 288–303.

[35] J. Hu, K.A. Kuttiyiel, K. Sasaki, C. Zhang, R.R. Adzic, Determination of hydrogen oxidation reaction mechanism based on Pt− Had energetics in alkaline electrolyte, J. Electrochem. Soc. 165 (2018) J3355.

[36] A.J. Bard, L.R. Faulkner, Fundamentals and applications, Electrochem. Methods 2 (2001) 580–632.

[37] F. Barbir, PEM fuel cells: theory and practice, Academic press, 2012.

[38] W. Sheng, M. Myint, J.G. Chen, Y. Yan, Correlating the hydrogen evolution reaction activity in alkaline electrolytes with the hydrogen binding energy on monometallic surfaces, Energy Environ. Sci. 6 (2013) 1509–1512.

[39] E. Cossar, M.S. Houache, Z. Zhang, E.A. Baranova, Comparison of electrochemical active surface area methods for various nickel nanostructures, J. Electroanal. Chem. 870 (2020), 114246.

[40] J. Zheng, Y. Yan, B. Xu, Correcting the hydrogen diffusion limitation in rotating disk electrode measurements of hydrogen evolution reaction kinetics, J. Electrochem. Soc. 162 (2015) F1470.

[41] T. Schmidt, H. Gasteiger, G. Stäb, P. Urban, D. Kolb, R. Behm, Characterization of high-surface-area electrocatalysts using a rotating disk electrode configuration, J. Electrochem. Soc. 145 (1998) 2354.

[42] W. Ni, A. Krammer, C.S. Hsu, H.M. Chen, A. Schüler, X. Hu, Ni3N as an active hydrogen oxidation reaction catalyst in alkaline medium, Angew. Chem. 131 (2019) 7523–7527.

[43] E. Chassaing, K.V. Quang, R. Wiart, Mechanism of nickel-molybdenum alloy electrodeposition in citrate electrolytes, J. Appl. Electrochem. 19 (1989) 839–844.

[44] R. Mousavi, M. Bahrololoom, F. Deflorian, L. Ecco, Improvement of corrosion resistance of Ni Mo alloy coatings: Effect of heat treatment, Appl. Surf. Sci. 364 (2016) 9–14.

[45] Y. Gao, H. Peng, Y. Wang, G. Wang, L. Xiao, J. Lu, L. Zhuang, Improving the antioxidation capability of the ni catalyst by carbon shell coating for alkaline hydrogen oxidation reaction, ACS Appl. Mater. Interfaces 12 (2020) 31575–31581.

[46] A.G. Oshchepkov, A. Bonnefont, E.R. Savinova, On the influence of the extent of oxidation on the kinetics of the hydrogen electrode reactions on polycrystalline nickel, Electrocatalysis 11 (2019) 133–142.

[47] A.P. Grosvenor, M.C. Biesinger, R.S.C. Smart, N.S. McIntyre, New interpretations of XPS spectra of nickel metal and oxides, Surf. Sci. 600 (2006) 1771–1779.

[48] S. Evans, J. Pielasze, J.M. Thomas, Oxidation of nickel studied by UV and X-ray photoelectron spectroscopy, Surf. Sci. 55 (1976) 644–662.

[49] M.C. Biesinger, L.W. Lau, A.R. Gerson, R.S. Smart, The role of the Auger parameter in XPS studies of nickel metal, halides and oxides, Phys. Chem. Chem. Phys. 14 (2012) 2434–2442.

[50] N. Weidler, J. Schuch, F. Knaus, P. Stenner, S. Hoch, A. Maljusch, R. Schäfer, B. Kaiser, W. Jaegermann, X-ray photoelectron spectroscopic investigation of plasma-enhanced chemical vapor deposited NiO x, NiO x (OH) y, and CoNiO x

(OH) y: influence of the chemical composition on the catalytic activity for the oxygen evolution reaction, The, J. Phys. Chem. C. 121 (2017) 6455–6463.

[51] H.-q Wang, X.-p Fan, X.-h Zhang, Y.-g Huang, Q. Wu, Q.-c Pan, Q.-y Li, In situ growth of NiO nanoparticles on carbon paper as a cathode for rechargeable Li–O 2 batteries, RSC Adv. 7 (2017) 23328–23333.

[52] M. Villa, E. Verardi, P. Salvi, P. Nelli, G. Zangari, Electrochemical activation of Raney nickel air electrodes, ECS Trans. 11 (2008) 105.

[53] J. Baltrusaitis, B. Mendoza-Sanchez, V. Fernandez, R. Veenstra, N. Dukstiene, A. Roberts, N. Fairley, Generalized molybdenum oxide surface chemical state XPS determination via informed amorphous sample model, Appl. Surf. Sci. 326 (2015) 151–161.

[54] G. Apai, J. Hamilton, J. Stohr, A. Thompson, Extended X-ray—absorption fine structure of small Cu and Ni clusters: binding-energy and bond-length changes with cluster size, Phys. Rev. Lett. 43 (1979) 165.

[55] I. Leontyev, A. Kuriganova, N. Leontyev, L. Hennet, A. Rakhmatullin, N. Smirnova, V. Dmitriev, Size dependence of the lattice parameters of carbon supported platinum nanoparticles: X-ray diffraction analysis and theoretical considerations, Rsc Adv. 4 (2014) 35959–35965.

[56] S. Medway, C. Lucas, A. Kowal, R. Nichols, D. Johnson, In situ studies of the oxidation of nickel electrodes in alkaline solution, J. Electroanal. Chem. 587 (2006) 172–181.

[57] P. Jiang, Y. Yang, R. Shi, G. Xia, J. Chen, J. Su, Q. Chen, Pt-like electrocatalytic behavior of Ru–MoO 2 nanocomposites for the hydrogen evolution reaction, J. Mater. Chem. A 5 (2017) 5475–5485.